ISSN 1392-1207. MECHANIKA. Vol. 32, No. 5, 2026: 389–401

Performance Analysis of 8W4L Wheel-Legged Hybrid Mobile Robot with Parallel Mechanism

Weiwei HU*, Ruiqin LI, Di LIN*****
**School of Mechanical Engineering, North University of China, Taiyuan, China,030051,*
E-mail: b20230201@st.nuc.edu.cn
***School of Mechanical Engineering, North University of China, Taiyuan, China,030051,*
E-mail: liruiqin@st.nuc.edu.cn (Corresponding Author)
****School of Mechanical Engineering, North University of China, Taiyuan, China,030051, E-mail: lindi@jzci.edu.cn*
https://doi.org/10.5755/j02.mech.45293

1. Introduction

With the continuous exploration of the natural world by humans, the scope of social industrial activities is constantly expanding. Mobile robots have been widely used in complex terrain environments such as field reconnaissance, post disaster rescue, and material handling. However, in the face of complex and ever-changing real environments, single wheeled or tracked movements are difficult to meet different working conditions. Therefore, common wheel leg composite mobile robots [1] and quadruped mobile robots [2] have emerged, which to some extent improve the terrain adaptation ability of robots and humans. Among various types of mobile robots, foot and leg foot mobile robots have a high ability to cross gullies and climb stairs due to their discrete foot end contact patterns. However, traditional serial leg mechanisms have characteristics such as accumulated error accuracy and slow response speed. The parallel mechanism, with its high load-bearing capacity and high motion accuracy, has demonstrated its outstanding advantages in precision machining and other fields [3-5]. Therefore, how to integrate parallel mechanisms with the field of mobile robots is currently a research hotspot of concern for many scholars.

There are two main applications of parallel mechanisms in the field of mobile robots. One approach is to view the parallel mechanism as a mobile robot and move it by deforming the configuration and posture of the parallel mechanism. Another approach is to use a parallel mechanism as the leg mechanism of a mobile robot, and achieve the robot's movement by changing the posture of the parallel mechanism movement platform. Currently, many scholars have conducted relevant research.

Tian et al. [6] designed a reconfigurable mobile parallel robot, which consists of a parallel mechanism and achieves various motion modes such as rolling, rolling, and quadrupedal walking by changing the mechanism configuration. Chai et al. [7] proposed a wheel leg mobile robot based on a reconfigurable parallel mechanism, which integrates three motion modes: hexapod walking, robotic arm operation, and wheeled movement through phase switching of reconfigurable joints. Gan et al. [8] proposed a novel mobile parallel robot that achieves both movement and operation functions through coordinated motion of a wheeled mobile base, and conducted systematic research on its configuration synthesis, kinematics, dynamics, and prototype verification. The research team of Takashi Chunfu from Waseda University [9-11] proposed a dynamic stiffness experimental method for bipedal walking robots based on cable measurement systems, as well as an unknown external force compensation control strategy that integrates ZMP feedback and foothold adjustment. Beijing Institute of Technology et al. [12-15] designed a large load parallel hexapod legged mobile robot called BIT-NAZA-II, mainly focusing on the stable walking problem of mobile robots in unstructured terrain. Gao et al. [16-19] designed the Octopus series of hexapod robots based on parallel mechanisms and conducted systematic research on their kinematic performance analysis, fault-tolerant motion planning, obstacle avoidance path planning, and sensorless adaptive gait generation. WANG et al. [20, 21] designed a manned walking chair robot based on a parallel leg mechanism, and conducted systematic research on its kinematics, workspace, dynamics, over actuated dynamic load optimization allocation, and composite position control strategy and experiments. Wu et al. [22] designed a six degrees of freedom parallel picking and placing robot called Hexad, which combines high rotational capability and simplified structure. Arm et al. [23] designed a dynamic quadruped robot SpaceBok for space exploration, focusing on jumping and gait in low gravity environments.

In summary, using a parallel mechanism as a mobile robot as a whole has low stability and small size. If a branch leg of the parallel mechanism fails, the mobile robot cannot work normally and has low terrain adaptability. Another approach to using parallel mechanisms as robot leg structures is mainly divided into independent leg structures and wheel leg structures with wheel trains added to the moving platform. This design concept mainly utilizes the heavy load and flexibility of parallel mechanisms, but if a group of parallel branch legs fails, it will also seriously affect the normal operation of the mobile robot.

Based on this, this article designs an 8W4L wheel leg composite mobile robot based on parallel mechanism. The second section proposes a specific 2-PUS&PRPR parallel mechanism configuration and establishes an analytical coordinate system. In the third section, the screw theory was used to analyze the degrees of freedom of the parallel mechanism, and the inverse kinematics equation of the parallel mechanism was established using the vector closed loop method. The fourth section analyzes the parallel performance from three aspects: workspace, singularity, and motion force transmission. The fifth section lists two arrangements of using parallel mechanisms as branch legs for mobile robots. Finally, gait planning and validation of mobile robots were carried out for typical cross gully terrain.

2. Configuration Analysis and Coordinate System Establishment

A novel 2-PUS&PRPR parallel mechanism is proposed based on a parallel mechanism. The specific configuration is shown in Fig. 1. The parallel mechanism consists of a fixed platform, a moving platform, and three connecting branches. The fixed platform includes a plane and two branch legs with omnidirectional wheels. The two branch legs are located at the two vertices of the plane rectangle. The flat design of the fixed platform is a square, and the moving platform is designed as an equilateral triangle. For the convenience of description, the fixed platform is divided into an upper platform and two branched legs. The upper platform is the plane on the fixed platform, and the moving platform is the lower platform. The three connecting branches consist of two PUS branches and one PRPR branch. An omnidirectional wheel is installed at the end of each of the two branched legs of the fixed platform, serving as the parallel mechanism wheel type moving body. The position of the lower platform in space is controlled by three connecting branches, and the lower platform serves as the main body of the legged mobile parallel mechanism.

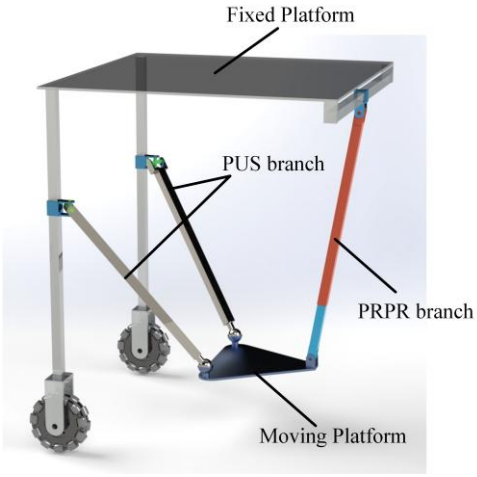

Fig. 1 2-PUS & PRPR parallel mechanism model

In order to facilitate the analysis of the parallel mechanism, a schematic diagram of the mechanism is drawn and a coordinate system is established, as shown in Fig. 2. Establish a fixed coordinate system O_1-$X_1Y_1Z_1$ on the upper platform, with the origin O_1 located at the geometric center of the squares $A_1A_2A_3A_4$ on the upper platform, X_1 pointing towards the midpoint of A_1A_3, Y_1 pointing towards the midpoint of A_3A_4, and Z_1 pointing upwards perpendicular to the upper platform. Establish a moving coordinate system O_2-$X_2Y_2Z_2$ on the lower platform, with X_2 direction along the base E_2E_1 of equilateral triangle $E_1E_2E_3$ on the moving platform, Z_2 pointing upwards perpendicular to the moving platform. According to the right-hand rule of the coordinate system, Y_2 is perpendicular to the base E_1E_2 and points towards vertex E_3. The square on the upper platform is represented by $A_1A_2A_3A_4$, the length of the side length in the positive direction is represented by a, the equilateral triangle on the lower platform is represented by $E_1E_2E_3$, and the side length of the equilateral triangle is represented by e. Two branch legs are fixedly installed at two points A_1 and A_2 on the upper platform, with omnidirectional wheels at the ends of the branch legs. Both branch legs serve as the main carriers for the prismatic pairs of the two PUS branches. The two branched legs are represented by A_1D_1 and A_2D_2 respectively, and the two PUS branches are represented by $B_1C_1E_1$ and $B_2C_2E_2$, where $B_1C_1E_1$ represents PUS-I branch and $B_2C_2E_2$ represents PUS-II branch. B_1 and B_2 are two prismatic pairs, C_1 and C_2 are two Hooke joints, and E_1 and E_2 are two spherical pairs connected to the lower platform. Design a prismatic pair B_3 on the A_3A_4 side of the upper platform, where $B_3C_3D_3E_3$ represents the PRPR branch and E_3 represents the connection between the revolute pair and the lower platform.

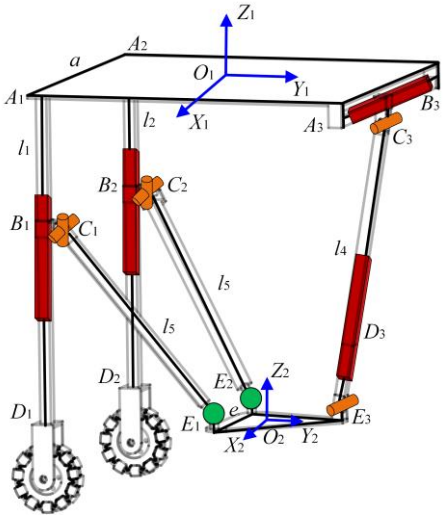

Fig. 2 Schematic diagram of 2-PUS & PRPR parallel mechanism

3. Kinematic Analysis

3.1. Degree of freedom analysis of the manipulator

The core application of a parallel mechanism is to determine its number of kinematic degrees of freedom. Therefore, it is necessary to identify the degrees of freedom before conducting in-depth research on a parallel mechanism. A parallel mechanism consists of a fixed platform and a moving platform, and the number of degrees of freedom of the moving platform relative to the fixed platform is defined as the degrees of freedom of the whole manipulator. Based on screw theory, the degrees of freedom of the novel 2-PUS&PRPR parallel mechanism are analyzed in this work. The three branches are investigated separately, and the constraints exerted by the end of each branch on the moving platform are superimposed to obtain the total degrees of freedom of the moving platform. First, the PUS branch is analyzed. A local coordinate system consistent with that in Fig. 2 is established at the prismatic pair of the PUS branch. The kinematic screw system of the PUS branch in this coordinate system can be expressed as

$$\begin{cases} \boldsymbol{S}_{11} = (0 \quad 0 \quad 0, 0 \quad 0 \quad 1) \\ \boldsymbol{S}_{12} = (1 \quad 0 \quad 0, 0 \quad 0 \quad 0) \\ \boldsymbol{S}_{13} = (0 \quad 0 \quad 1, 0 \quad 0 \quad 0) \\ \boldsymbol{S}_{14} = (1 \quad 0 \quad 0, 0 \quad e_{41} \quad f_{41}) \\ \boldsymbol{S}_{15} = (0 \quad 1 \quad 0, -e_{41} \quad 0 \quad 0) \\ \boldsymbol{S}_{16} = (0 \quad 0 \quad 1, -f_{41} \quad 0 \quad 0) \end{cases}. \tag{1}$$

According to the reciprocal product relationship between motion and constraints in screw theory, Eq. (1) is calculated to have a rank of 6 and there is no constraint screw. Therefore, the PUS branch has six degrees of freedom. When studying the PRPR branch, a sub coordinate system is also established on the prismatic pair connected to the fixed platform, with the direction consistent with the coordinate direction in Fig. 2. The motion screw system of the PRPR branch can be obtained as follows:

$$\begin{cases} \boldsymbol{S}_{21} = (0 \quad 0 \quad 0, 1 \quad 0 \quad 0) \\ \boldsymbol{S}_{22} = (1 \quad 0 \quad 0, 0 \quad 0 \quad 0) \\ \boldsymbol{S}_{23} = (0 \quad 0 \quad 0, 0 \quad e_{32} \quad f_{32}) \\ \boldsymbol{S}_{24} = (1 \quad 0 \quad 0, 0 \quad e_{42} \quad f_{42}) \end{cases}. \tag{2}$$

Based on the reciprocal product of kinematic screws and constraint screws in screw theory, the rank of Eq. (2) is calculated to be 4, and there exist two reciprocal screws as follows.

$$\begin{cases} \boldsymbol{S}_{21}^{r} = (0 \quad 0 \quad 0, 0 \quad 1 \quad 0) \\ \boldsymbol{S}_{22}^{r} = (0 \quad 0 \quad 0, 0 \quad 0 \quad 1) \end{cases}. \tag{3}$$

According to Eq. (3), the PRPR branch is constrained by two directions of force couples, meaning that the end of the branch cannot rotate along the *Y*-axis and *Z*-axis. In summary, for the 2-PUS&PRPR parallel mechanism, the two PUS branches have no constraints on the moving platform, while the PRPR branch has three constraints on the moving platform. Therefore, the parallel mechanism as a whole has four degrees of freedom, with movement along the *XYZ* directions and rotation around the *X*-axis.

According to the revised G-K formula, the degrees of freedom of the 2-PUS&PRPR parallel mechanism are verified, and the specific equation is as follows

$$M = d(n - g - 1) + \sum_{i=1}^{g} f_i + v - \delta, \tag{4}$$

where: the order of the parallel mechanism $d = 6$, the total number of links including the frame $n = 9$, and the number of kinematic pairs $g = 10$. All kinematic pairs contribute 16 degrees of freedom. There are no redundant constraints $v = 0$ and local degree of freedom $\delta = 0$. Substituting these parameters into the formula, the degrees of freedom M is derived as:

$$M = 6(9 - 10 - 1) + 16 + 0 - 0 = 4. \tag{5}$$

Based on the above analysis and verification, it can be determined that the 2-PUS&PRPR parallel mechanism has a total of 4 spatial degrees of freedom.

3.2. Inverse kinematics analysis

The kinematic calculation of parallel mechanisms can be divided into forward solution analysis and inverse solution analysis. Forward solution analysis involves solving the pose parameters of the end effector based on the known parameters of the driving element, while inverse solution analysis involves inferring the input parameters of the driving element based on the known pose parameters of the end effector. Positive solution analysis is commonly used for kinematic analysis of serial robots. Parallel mechanisms, due to having multiple connecting branches, use forward solution operations. When there is a unique driving input parameter, there may be more than one possibility for the end effector, which is the problem of multiple solutions. Therefore, inverse solution analysis is used for the kinematic analysis of parallel mechanisms. Assuming that the pose parameters of the geometric centre of the lower platform of the 2-PUS&PRPR parallel mechanism are (x y z, α β γ), which represent the three movements and three rotations of the end effector in the mechanism's coordinate system, respectively, the driving variation can be solved through computation. Due to the four degrees of freedom of the parallel mechanism, four drivers are required, using the moving pair in the three branches as the driver. As shown in Fig. 2, due to the movement of the prismatic pairs of the two PUS branches on the legs of the two branches, the moving pair connected to the PRPR branch and the upper platform moves along one side of the square of the upper platform. Based on this mechanism, $A_1B_1 = l_1$, $A_2B_2 = l_2$, $A_3B_3 = l_3$, $C_3E_3 = l_4$ are set. In addition, the side length of the square of the upper platform is represented by a, and the side length of the equilateral triangle of the lower platform is represented by e, $C_1E_1 = C_2E_2 = l_5$。 Based on the above settings, the representation of different points on the platform in the fixed coordinate system can be obtained as

$$\begin{cases} {}^{O_1}A_1 = \begin{bmatrix} \frac{a}{2} & -\frac{a}{2} & 0 \end{bmatrix}^T & {}^{O_1}A_2 = \begin{bmatrix} -\frac{a}{2} & -\frac{a}{2} & 0 \end{bmatrix}^T \\ {}^{O_1}A_3 = \begin{bmatrix} \frac{a}{2} & \frac{a}{2} & 0 \end{bmatrix}^T & {}^{O_1}A_4 = \begin{bmatrix} -\frac{a}{2} & \frac{a}{2} & 0 \end{bmatrix}^T \end{cases}. \tag{6}$$

In addition, the coordinate representation of the motion pair connected to the fixed platform by the three branches can be obtained

$$\begin{cases} {}^{O_1}\boldsymbol{B}_1 = {}^{O_1}\boldsymbol{C}_1 = \begin{bmatrix} \frac{a}{2} & -\frac{a}{2} & -l_1 \end{bmatrix}^T \\ {}^{O_1}\boldsymbol{B}_2 = {}^{O_1}\boldsymbol{C}_2 = \begin{bmatrix} -\frac{a}{2} & -\frac{a}{2} & -l_2 \end{bmatrix}^T \\ {}^{O_1}\boldsymbol{B}_3 = {}^{O_1}\boldsymbol{C}_3 = \begin{bmatrix} \frac{a}{2} - l_3 & \frac{a}{2} & 0 \end{bmatrix}^T \end{cases}. \tag{7}$$

The coordinates of each point on the platform in the dynamic coordinate system are represented as

$$\begin{cases} {}^{O_2}\boldsymbol{E}_1 = \begin{bmatrix} \frac{e}{2} & -\frac{\sqrt{3}e}{6} & 0 \end{bmatrix}^T \\ {}^{O_2}\boldsymbol{E}_2 = \begin{bmatrix} -\frac{e}{2} & -\frac{\sqrt{3}e}{6} & 0 \end{bmatrix}^T \\ {}^{O_2}\boldsymbol{E}_3 = \begin{bmatrix} 0 & \frac{\sqrt{3}e}{3} & 0 \end{bmatrix}^T \end{cases}. \tag{8}$$

The coordinate transformation of the moving coordinate system relative to the fixed coordinate system follows the *X*-*Y*-*Z* sequence. The corresponding transformation matrix is presented below:

$$\boldsymbol{T}=\begin{bmatrix} c_\beta c_\gamma & s_\alpha s_\beta c_\gamma - c_\alpha s_\gamma & c_\alpha s_\beta c_\gamma + s_\alpha s_\gamma \\ c_\beta s_\gamma & s_\alpha s_\beta s_\gamma + c_\alpha c_\gamma & s_\alpha s_\beta s_\gamma - s_\alpha c_\gamma \\ -s_\beta & s_\alpha c_\beta & c_\alpha c_\beta \end{bmatrix}. \tag{9}$$

Here and further in the equations c_α denotes $cos(\alpha)$; $c_\beta = cos(\beta)$; $c_\gamma = cos(\gamma)$; s_α denotes $sin(\alpha)$; $s_\beta = sin(\beta)$; $s_\gamma = sin(\gamma)$. Accordingly, the coordinates of points on the moving platform in the fixed coordinate system after coordinate transformation can be expressed as:

$$^{O_1}\boldsymbol{E}_i = \boldsymbol{T}\cdot {}^{O_2}\boldsymbol{E}_i + \boldsymbol{P}\ . \tag{10}$$

The $\boldsymbol{P}$ in the equation represents the relative position of the origin of the moving coordinate system with respect to the static coordinate system, where the value of i is 1, 2, and 3. Since it is known in the previous text that the mechanism's moving platform has four degrees of freedom, including three movements and one rotation around the *X*-axis direction, it can be inferred that the values of β and γ in Eq. (9) are both 0. By substituting them, Eq. (9) becomes

$$\boldsymbol{T}=\begin{bmatrix} 1 & 0 & 0 \\ 0 & c_\alpha & -s_\alpha \\ 0 & s_\alpha & c_\alpha \end{bmatrix}. \tag{11}$$

Substituting Eq. (11) and Eq. (8) into Eq. (10), the coordinates of each point on the lower platform in the fixed coordinate system are obtained as:

$$\begin{cases} {}^{O_1}\boldsymbol{E}_1 = \left[\dfrac{e}{2}+x \quad -\dfrac{\sqrt{3}e}{6}\bullet c_\alpha + y \quad -\dfrac{\sqrt{3}e}{6}\bullet s_\alpha + z\right]^T \\ {}^{O_1}\boldsymbol{E}_2 = \left[-\dfrac{e}{2}+x \quad -\dfrac{\sqrt{3}e}{6}\bullet c_\alpha + y \quad -\dfrac{\sqrt{3}e}{6}\bullet s_\alpha + z\right]^T \\ {}^{O_1}\boldsymbol{E}_3 = \left[x \quad \dfrac{\sqrt{3}e}{3}\bullet c_\alpha + y \quad \dfrac{\sqrt{3}e}{3}\bullet s_\alpha + z\right]^T \end{cases}. \tag{12}$$

Since the moving platform has no rotation about the *Y*-axis or *Z*-axis, and restricted by the mechanism configuration, the coordinate X_1 of the kinematic pairs in the PRPR branch in the fixed coordinate system is equal to the *x*-coordinate of the origin of the moving platform coordinate system. Therefore, we can obtain:

$$\begin{cases} l_3 = \dfrac{e}{2} - x \\ l_4 = \left| {}^{O_1}\boldsymbol{C}_3\overrightarrow{{}^{O_1}\boldsymbol{E}_3} \right| \end{cases}. \tag{13}$$

Furthermore, given that the connecting rod $C_1E_1 = C_2E_2 = l_5$, it can be concluded that

$$l_5 = \left| {}^{O_1}\boldsymbol{C}_1\overrightarrow{{}^{O_1}\boldsymbol{E}_1} \right| = \left| {}^{O_1}\boldsymbol{C}_2\overrightarrow{{}^{O_1}\boldsymbol{E}_2} \right|. \tag{14}$$

By combining Eq. (7), the length representations of l_1 and l_2 can be obtained. The above Eqs. (13) and (14) are the inverse equations for the 2-PUS&PRPR parallel mechanism. Four driving parameters l_i (i = 1, 2, 3, 4) can be obtained by combining the parameters (x, y, z, α, 0, 0) of the end components of the parallel mechanism.

4. Kinematic Performance Analysis and Optimization

4.1. Workplace analysis

The workspace is an important core performance indicator of parallel mechanisms, which represents the set of all possible poses that can be achieved by the end effector of the parallel mechanism in space. It can serve as an important basis for the reachable range of the parallel mechanism, the limit of the motion process, and the adaptation of the application scenario. The parallel mechanism has multiple connecting branches, forming multiple closed-loop coupled branch constraints. Therefore, it is subject to various constraints including the expandable length of the members, the reachable range of the motion pair, and the interference between the members. Most parallel mechanisms have characteristics such as irregular shape and limited effective working area. Therefore, in order to verify the application of parallel mechanisms in the field of mobile robots, it is necessary to analyse their reachable workspace. In order to improve the authenticity of verification, based on the application field of mobile robots, its parameters are initially set, and its workspace is analysed based on these parameters. The preliminary setting is that the side length a of the square on the upper platform is 600mm, and the equilateral triangle on the lower platform is 230mm. Considering that the mobile robot has omnidirectional wheels at the lower ends of the two branch legs, the length l_5 of the two PUS branches is set to 600mm, and the movement trajectory range of these two PUS branch prismatic pairs is 600 mm, that is, $A_1D_1 = A_2D_2 = 600$ mm. In addition, the length range of the middle prismatic pair of the PRPR branch is between [600, 1200]. The workspace of the 2-PUS&PRPR parallel linkage platform is shown in Fig. 3.

The workspace visualization of the 2-PUS&PRPR parallel mechanism is shown in Fig. 3, where Fig. 3, a is a three-dimensional view of the workspace. It can be observed that under the initial parameters, the parallel mechanism operates within the workspace range of $X \in [-300\text{ mm}, 300\text{ mm}]$, $Y \in [-300\text{ mm}, 300\text{ mm}]$, and

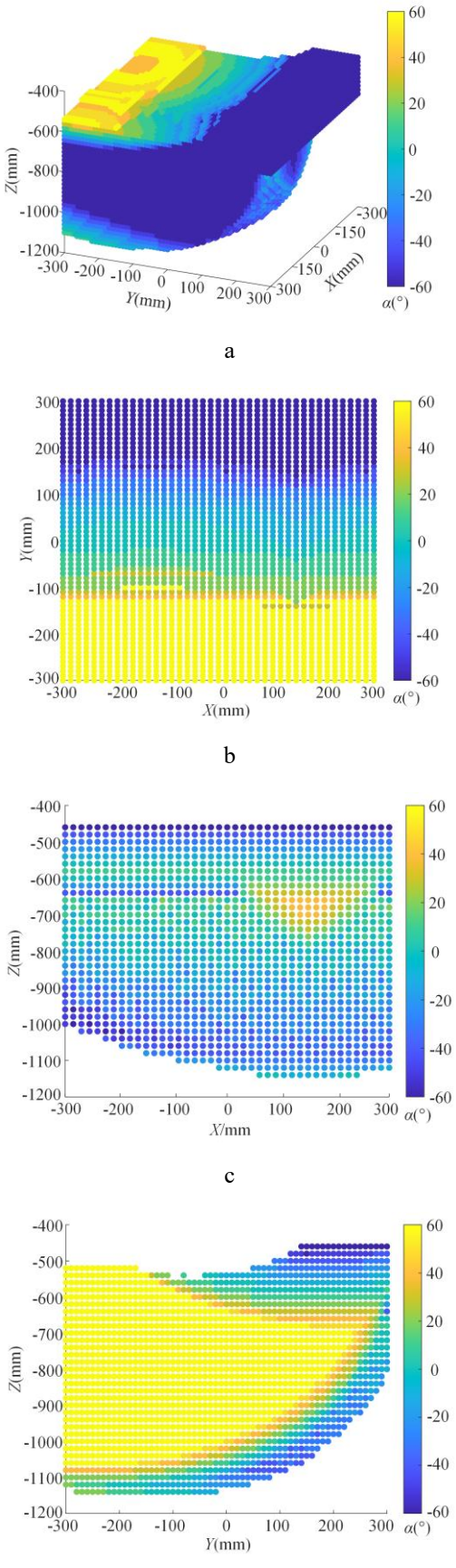

Fig. 3 Workspace of 2-PUS & PRPR parallel mechanism: a – 3D workspace, b – workspace on X-Y plane at $Z = -800$, c – workspace on X-Z plane at $Y = 0$, d – workspace on Y-Z plane at $X = 0$

$Z \in [-400\text{ mm}, -1200\text{ mm}]$. Based on coordinate establishment, the smaller the Z-axis value, the farther the distance between the lower platform and the upper platform, and the greater the displacement ability in the X-axis and Y-axis directions. This proves that the parallel mechanism has strong attitude adjustment ability in terms of height, which can meet the support and leg lifting actions of mobile robots. Due to the initial design of two omnidirectional wheel branch leg lengths and omnidirectional wheel dimensions, the workspace in the X-Y plane is analysed when $Z = -800$ mm, as shown in Fig. 3, b. At this point, the mechanism is at the midpoint support height of the branch leg and can cover all spaces under the upper platform. This proves that the mechanism has good attitude adjustment ability under support conditions, reducing the risk of overturning of the mobile robot. In Fig. 3, c, the distribution of reachable points in the X-Z plane is continuous, without singular boundaries or obvious voids. The mechanism does not have active dead points when moving in the forward and backward directions. Fig. 3, d shows the workspace in the Y-Z plane when $X = 0$, which has an asymmetric distribution characteristic. However, its reachable range in the $Y \in [-300\text{ mm}, 0\text{ mm}]$ region is significantly larger than that in the $Y \in [0\text{ mm}, 300\text{ mm}]$ region. It can still cover the range of $Y \in [-300\text{ mm}, 300\text{ mm}]$ at a median height of -800 mm, and can operate up to -1100 at a height of $Y \in [-300\text{ mm}, 0\text{ mm}]$, which can assist the robot in completing obstacle crossing functions and improve its obstacle crossing ability.

In summary, the workspace of the 2-PUS&PRPR parallel mechanism can be highly matched with the movement requirements of the branch as a mobile robot. The mechanism has stable posture adjustment ability when supported at a low position, and can achieve support at different heights; When completing high-level leg lifting, the mechanism has a large horizontal movement ability, which can meet the requirements of obstacle crossing and complex turning movements. At the same time, the workspace of the institution does not have obvious singular configurations and has continuity, which can ensure the stability of the robot during movement.

4.2. Singularity analysis of parallel mechanism

The singular configuration of a parallel mechanism refers to the phenomenon where the motion and force transmission characteristics of the mechanism undergo sudden changes, the degrees of freedom undergo instantaneous changes, the force on the components of the mechanism increases sharply, and the control becomes ineffective under a specific configuration. Singular analysis is a core indicator for studying the performance of parallel mechanisms, therefore, the following singularity analysis is conducted on the 2-PUS&PRPR parallel mechanism. The pose parameters of the mechanism's moving platform are represented as $v = [x, y, z, \alpha]^T$, and the four drives of the parallel mechanism are represented as $q = [l_1, l_2, l_3, l_4]^T$. Based on the inverse solution equation in the previous text, four independent constraint equations can be obtained. By taking their derivatives, the mapping relationship between the speed of the moving platform and the speed of the driving components can be obtained

$$\boldsymbol{G}\dot{\boldsymbol{v}} = \boldsymbol{J}\dot{\boldsymbol{q}}\,. \tag{15}$$

In the formula, $\boldsymbol{G}$ represents the output Jacobian matrix of the parallel mechanism, and $\boldsymbol{J}$ represents the drive input Jacobian matrix. These two Jacobian matrices can be obtained based on the inverse kinematics solution. Due to the design structural characteristics, l_i (i = 1, 2, 3) may be zero. However, if it is zero, it will directly cause the input Jacobian matrix to be singular. Therefore, in control, it is necessary to avoid the situation where l_i (i = 1, 2, 3) is zero. Under this premise, the input Jacobian matrix is an identity matrix, and the output Jacobian matrix can be represented as

$$\boldsymbol{G} = \begin{bmatrix} G_{11} & G_{12} & G_{13} & G_{14} \\ G_{21} & G_{22} & G_{23} & G_{24} \\ G_{31} & G_{32} & G_{33} & G_{34} \\ G_{41} & G_{42} & G_{43} & G_{44} \end{bmatrix}. \tag{16}$$

When the input and output Jacobian matrices approach singularity, the parallel mechanism will experience singularity. We have analyzed the input singularity to avoid situations where l_i (i = 1, 2, 3) is 0. When analyzing the output Jacobian matrix, that is, the condition for the singularity of the mechanism to occur is $det(\boldsymbol{G})$ = 0, the values of the $\boldsymbol{G}$ matrix can be derived by inverse solving the equation, and finally obtained

$$det(\boldsymbol{G}) = -(G_{22} - G_{12})(G_{44} + G_{14}G_{43})\,. \tag{17}$$

Through calculation, in order to gain a clearer understanding of the occurrence of singularities, this article innovatively uses logarithmic form $lg|det(\boldsymbol{G})|$ to determine the trend of the determinant value of the output Jacobian matrix approaching 0. The mechanism parameters refer to the parameters mentioned earlier, as shown in Fig. 4.

Using logarithmic form to reflect singular performance to some extent avoids the phenomenon of data being too large. Using $lg|det(\boldsymbol{G})|$ equivalence to observe the changes in singular values, darker colors represent smaller values of the determinant, and the mechanism is also close to singularity. The singular distribution diagram of the 2-PUS&PRPR parallel mechanism is shown in Fig. 4. Fig. 4, a shows the display of singular values in three-dimensional space. It can be observed that most of them are in the non-singular range, but there are two lines that may appear singular throughout the workspace. One is the plane when X = 0, and the other area is mainly concentrated around Y = –235 mm; Fig. 4, b shows that when Z = –800 mm and the rotation angle of the moving platform α = 0°, the singular region is mainly concentrated on the negative half axis

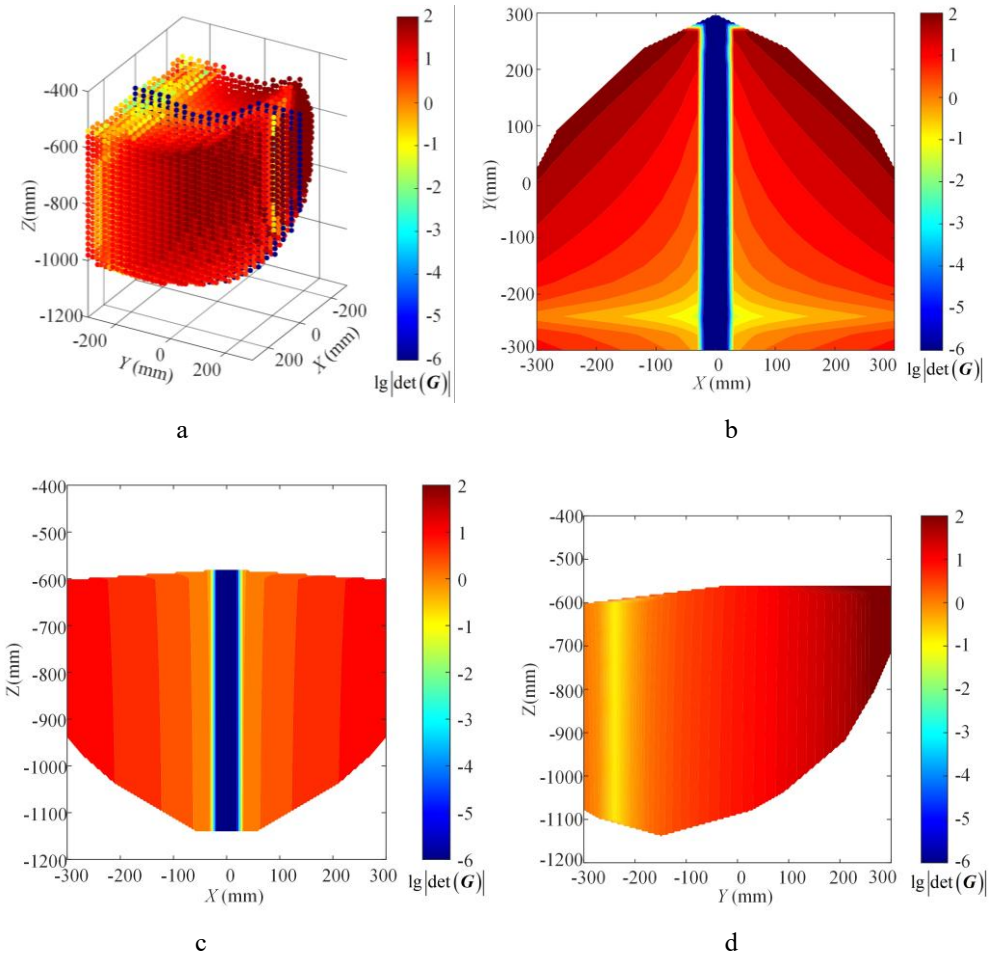

Fig. 4 The dexterity atlases Singularity distribution of 2-PUS & PRPR parallel mechanism: a – distribution of $lg|det(\boldsymbol{G})|$ values in three-dimensional space, b – distribution of $lg|det(\boldsymbol{G})|$ values on the X-Y plane at Z =–800 and α = 0°, c – distribution of $lg|det(\boldsymbol{G})|$ values on the X-Z plane at Y = 0 and α = 0°, d – distribution of $lg|det(\boldsymbol{G})|$ values on the Y-Z plane at X = 200 and α = 0°

of the *Y*-axis, presenting a "cross shaped" region, proving the existence of two perpendicular intersecting singular regions at $X = 0$ mm and near $Y = -235$ mm; Fig. 4, c shows the distribution of singular values when $Y = -150$ mm and the rotation angle of the moving platform $\alpha = 0°$. It can be clearly seen that the straight line along $X = 0$ does not change with height, indicating that the inherent singularity of the structure at that time is not the boundary singularity in the working space of the mechanism; Due to the previous analysis that $X = 0$ will cause singularity in the mechanism, the distribution of singular values in the *YOZ* plane when $X = 50$ and the rotation angle of the moving platform α=0 ° is analyzed in Fig. 4, d. It can be seen that there is still a singular region at $Y = -235$ mm. Based on the above analysis, it can be concluded that in order to ensure that parallel mechanisms do not experience singularities during motion, it is necessary to avoid singular configurations as much as possible. Firstly, ensure that the length dimension of the driving link is not zero. Additionally, set the upper and lower platform dimensions as large as possible. Finally, avoid passing through the inherent singular areas of the parallel mechanism, but it can be observed that the areas where singularities may occur are very narrow.

Applying this parallel mechanism to the field of mobile robots requires adjusting the pose and movement of the platform to enable the robot to move in complex terrains. As for the workspace at $Y = -235$ mm, it can be avoided as much as possible according to the previous text. However, the range corresponding to $X = 0$ is indeed an important neutral plane for mobile robots during the movement process. Therefore, in order to avoid singularity in the mechanism, redundant drives will be added to the design. When the lower platform passes through the singular plane, it will act smoothly to pass through the singular plane, and then the redundant drive will be turned off to achieve the parallel mechanism as the branch leg of the mobile robot.

4.3. Motion/force transmission performance analysis

The motion/force transmission performance of a mechanism can directly reflect the transmission efficiency of the driving energy of the mechanism to the effective output of the moving platform, which is an important indicator for measuring the load-bearing capacity and motion stability of parallel mechanisms. The Jacobian matrix can also be used to analyse the motion force transmission performance of parallel mechanisms, but to avoid tedious calculations, the input/output transmission index method of screw theory is adopted this time [24-26].

The parallel mechanism studied in this article is a non-redundant drive mechanism with four drive joints. The transmission index is defined below. The input transmission index λ_i, output transmission index η_i, and local transmission index Γ of the *i*-th drive branch are defined as

$$\lambda_i = \frac{\left|\$_{Ti} \circ \$_{Ii}\right|}{\left|\$_{Ti} \circ \$_{Ii}\right|_{max}}, \tag{18}$$

$$\eta_i = \frac{\left|\$_{Ti} \circ \$_{Oi}\right|}{\left|\$_{Ti} \circ \$_{Oi}\right|_{max}}, \tag{19}$$

$$\Gamma = min\left\{\lambda_i, \eta_i\right\}. \tag{20}$$

In the formula, $\$_{Ii}$ refers to the input twist screw of the parallel mechanism driving branch *i*, $\$_{Ti}$ refers to the transmission wrench screw acting on the moving platform after locking the driving branch *i*, $\$_{Oi}$ is the output twist screw of the moving platform while retaining the driving branch *i*. The "o" in the formula represents the reciprocal product in the screw theory. The various indicators in the above equation are dimensionless parameters with a value range of [0, 1]. The closer they are to 1, the higher the energy transfer efficiency of the driving joint.

The parallel mechanism consists of two PUS branches and one PRPR branch. Using the parameter properties mentioned earlier, the fixed platform is a square with a side length of 600mm, and the moving platform is an equilateral triangle with a side length of *e*. Referring to the coordinate resume method in Fig. 2, the driving force of the two PUS branches is a prismatic pair, and the axis of this prismatic pair is along the *Z*-axis direction. Therefore, its input twist screw is a pure moving pair

$$\$_{Ii} = \left(0 \quad 0 \quad 0, 0 \quad 0 \quad 1\right) \quad i = 1, 2. \tag{21}$$

After locking this actuator, the remaining Hooke joint (U-pair) and spherical joint (S-pair) form a set of constraint screws. Their lines of action are along the *Z*-axis and pass through the center of spherical joint E_i (i =1, 2). Accordingly, the transmission wrench screw is expressed as:

$$\$_{Ti} = \left(0 \quad 0 \quad 1, \boldsymbol{r}_{Ei} \times \boldsymbol{e}_z\right) \quad i = 1, 2. \tag{22}$$

The $\boldsymbol{r}_{Ei}$ in the above equation represents the position vector of the spherical pair E_i in the static coordinate system. When only a single PUS is used to drive its function and other drives are locked, the moving platform only moves along the *Z*-axis, so the output twist screw can be obtained as

$$\$_{Oi} = \left(0 \quad 0 \quad 0, 0 \quad 0 \quad 1\right). \tag{23}$$

In addition, analyzing the PRPR branch, which has two mobile drivers, we still refer to the data mentioned earlier. For the convenience of understanding, the connected driving prismatic pair is divided into P_1 and P_2 to represent. The input motion corresponding to P_1 can be obtained as a screw prismatic pair along the *X*-axis

$$\$_{I3} = \left(0 \quad 0 \quad 0, 1 \quad 0 \quad 0\right). \tag{24}$$

After locking all other drives, P_1 is also locked. At this time, the transmission wrench of the branched platform screws along the axis direction, which can be obtained

$$\$_{T3} = \$_{I3}. \tag{25}$$

Similarly, it can be inferred that for driving P_2, the input twist screw direction along the direction of the telescopic rod is represented as

$$\boldsymbol{u}_4 = \frac{\boldsymbol{E}_3 - \boldsymbol{C}_3}{l_4}. \tag{26}$$

The input twist screw can be obtained as

$$\$_{I3} = (0 \quad 0 \quad 0, \boldsymbol{u}_4) \ . \tag{27}$$

Similarly, it can be inferred that when P_2 is driven alone, the transmission wrench of the screw blade follows the $\boldsymbol{u}_4$ direction, and $\$_{T4} = \$_{I4}$.

By solving the output twist screw of the PRPR branch, the relationship between the displacement of the moving platform along the Z-axis direction and l_4 can be obtained through the inverse solution of motion. By taking the derivative of it with respect to z, the sensitivity of the length change driven by P_2 to the motion along the Z-axis can be obtained. After normalization calculation, the output transfer index η_4 can be directly calculated as

$$\eta_4 = \left|\frac{\partial l_4}{\partial z}\right| = \frac{\left|z + \left(\sqrt{3}e/3\right) \bullet \sin\alpha\right|}{l_4} \ . \tag{28}$$

For driving P_1, the corresponding output motion direction remains along the X-axis direction, consistent with the screw direction of its own transmission, thus obtaining $\eta_3 = 1$. The output transmission index of the other two PUS branches is $\eta_1 = \eta_2 = 1$, and the corresponding input transmission index is $\lambda_1 = \lambda_2 = 1$. Therefore, the local transmission index of the entire parallel mechanism can be obtained as follows:

$$\Gamma = min\{\eta_1, \eta_2, \eta_3, \eta_4\} = \eta_4 \ . \tag{29}$$

Based on the parallel mechanism model mentioned earlier, simulation examples can be used to obtain the motion/force transmission performance of the 2-PUS&PRPR parallel mechanism shown in Fig. 5.

Fig. 5, a shows the three-dimensional performance distribution of the workspace, which can visually present the distribution of local motion/force transmission performance. In the area near the upper motion boundary $Z \in$ [–400 mm, –600 mm] of the mechanism, the value of Γ is between 0.6-0.7, which belongs to the low performance region. The motion/force transmission efficiency of the mechanism is low in this region. As the Z value continues to decrease, its Γ rapidly increases. When the Z value is below –800 mm, the local transmission index is generally higher than 0.9, and the core region can reach 0.95 or above, which is a high-performance region. This indicates that the motion/force transmission performance efficiency of the mechanism in this region is high and the motion/force transmission performance is better. Fig. 5, b shows the distribution of motion/force transmission performance in the XOY plane when the Z value is –800 mm. It can be observed that in the region of $Y \in$ [–300 mm, –200 mm], the Γ value is in the range of 0.82-0.86, and the relative performance is the worst. This coincides with the singular analysis structure of the parallel mechanism. As the Y value continues to increase, the local performance index stabilizes between 0.94-0.96 within the range of $Y \in$ [–300 mm, 300 mm], indicating the best performance within this range. In addition, the change in X value has a weak impact on performance. At the same height of Y value, the lateral fluctuation of X value with the change of X value is very small, indicating that the change in Y direction is the main factor affecting the transmission performance of this parallel mechanism at the same

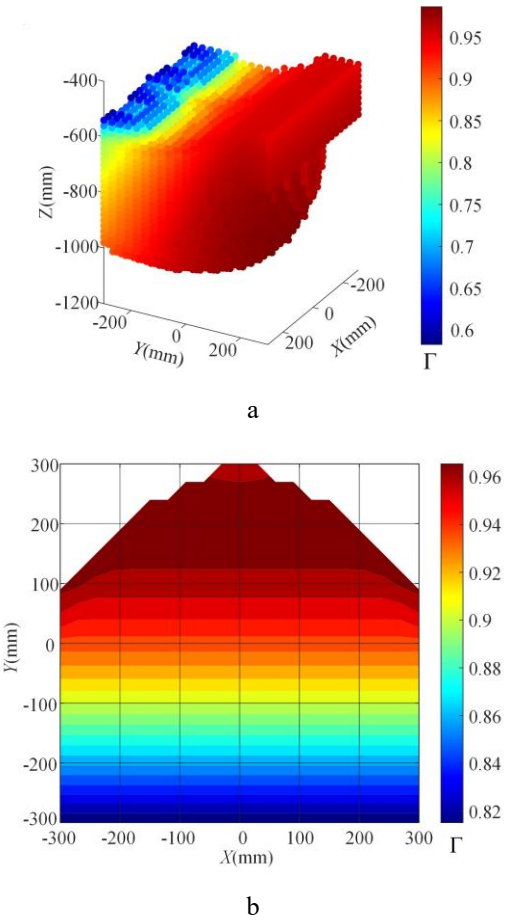

Fig. 5 Force transmission performance diagram: a – force transmission performance in the workspace, b – force transmission performance at $Z = -800$

height of Z value.

The local transmission index Γ only reflects the performance of a parallel mechanism in a certain configuration. In order to evaluate the transmission performance of the entire reachable workspace of the parallel mechanism, the global average transmission index ζ and the global fluctuation transmission index $\bar{\zeta}$ are defined, which specifically represent

$$\zeta = \frac{\int_W \Gamma dW}{\int_W dW} \ , \tag{30}$$

$$\bar{\zeta} = \frac{\int_W \Gamma \sqrt{\left(\Gamma - \zeta\right)^2} dW}{\int_W dW} \ , \tag{31}$$

where W denotes the reachable workspace. Further setting the comprehensive motion/force performance index $\psi = \left(1 - \bar{\zeta}\right)\zeta$ can reflect the stability of the average transmission efficiency and performance changes of the parallel mechanism, with a value range of [0, 1]. The larger the value obtained, the better the overall performance of the mechanism. By calculation, the global average transmission index of the parallel mechanism is $\zeta = 0.7326$, the fluctuation index $\bar{\zeta} = 0.0854$, and the comprehensive performance is $\psi = 0.6701$. Its comprehensive performance index is greater

than 0.5, indicating excellent global motion/force transmission performance and high efficiency.

5. Parallel Mechanism Applied to Mobile Robots

Installing the 2-PUS&PRPR parallel mechanism as a branch leg on an 8W4L wheel leg composite mobile robot can greatly improve the mobile performance of the robot by taking advantage of the high load-bearing capacity and low error of the parallel mechanism. The arrangement of branched legs in the main body of a mobile robot will to some extent affect the mechanical characteristics and motion coordination of the entire mechanism. The eight wheels in the 8W4L wheel leg composite mobile robot adopt omnidirectional wheels, which can greatly improve the maneuverability of the mobile robot in wheeled motion mode based on the characteristic of being able to move in any direction within the omnidirectional wheel plane. The proposed parallel mechanism can only be used as a part of moving the entire mobile robot, with one group consisting of a single parallel mechanical leg and the entire wheel leg composite mobile robot requiring multiple sets of parallel mechanisms. Based on this characteristic and application scenarios, two arrangement methods are proposed, namely symmetrical arrangement and circumferential sequential arrangement, which provide theoretical basis for subsequent gait design.

5.1. Oppositely symmetric arrangement

The symmetrical arrangement in the opposite direction is to arrange multiple sets of parallel branch legs in a relatively symmetrical manner, as shown in Fig 6. The upper platform of the parallel branch legs is installed at the lower end of the load platform, and four sets of parallel branch legs are installed respectively, distributed on both sides of the load platform. The specific structure refers to the layout diagram in the lower right corner of Fig. 6, which is a top view of the structure of the mobile robot. The circle represents the position of the omnidirectional wheel arrangement and the connecting end of the two PUS prismatic pairs. The square block represents the prismatic pair connected to the stationary platform in the PRPR branch. This arrangement of parallel branch legs is evenly distributed and can achieve mutual balance in space. This arrangement can ensure that the robot can still rely on the symmetrical layout when lifting a single leg. Stability. At the same time, the eight omnidirectional directions are divided into two groups, with one group consisting of four arranged on both sides of the load-bearing platform, forming a multi-point support system for the robot, improving its contact envelope area with the ground, and effectively enhancing the robot's anti overturning ability. When the robot is a wheeled obstacle, it has eight omnidirectional wheels, which combine stability and heavy load capacity; When the robot moves in a legged manner, it is supported by four sets of parallel branched legs, and the parallel mechanism has high load-bearing performance. Each set of branched legs has three connecting branches, which means that the robot also has extremely high stability and heavy load capacity in the legged movement state.

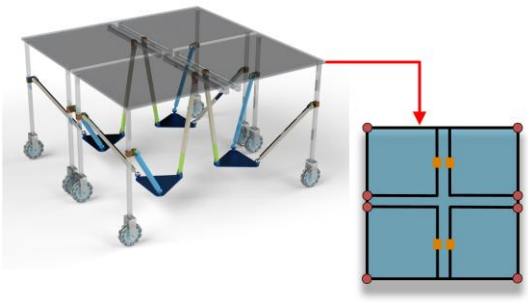

Fig. 6 Oppositely symmetrical arrangement

5.2. Circumferential sequential arrangement

The symmetrical arrangement of eight omnidirectional wheels is installed on both sides of the load platform, while there are no front or rear wheels. Its stability will also be affected in special moving scenarios. Therefore, a circumferential sequential arrangement is proposed, in which parallel branch legs are arranged in a clockwise square at the lower end of the load platform. As shown in Fig. 7, there are three omnidirectional wheels supporting each of the four directions of the load platform. Based on the motion performance of the omnidirectional wheels, it can move in any direction in the plane. Therefore, it can be installed according to the actual orientation in the figure. For each of the three omnidirectional wheels, two of them are installed in the same direction, and the third one is perpendicular to the first two. This arrangement method does not have strict symmetry constraints, and it has advantages in stability and maneuverability. The possibility of interference between two parallel branched legs is lower than that of a symmetrical arrangement.

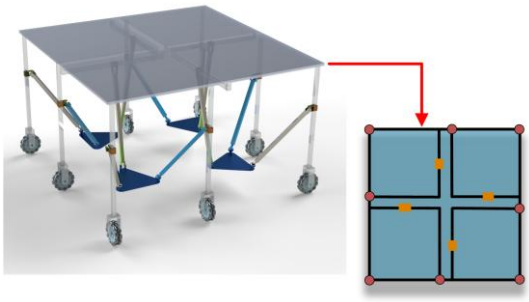

Fig. 7 Circumferential sequential arrangement

In summary, the symmetrical arrangement of eight omnidirectional wheels on both sides reduces the impact of omnidirectional wheel branches on obstacle crossing to a certain extent. The eight omnidirectional wheels have consistent orientations, reducing the difficulty of controlling their design. At the same time, the orientation of the four parallel branched legs is consistent, making the gait planning logic more concise. The circumferential sequential arrangement breaks the symmetry constraint, and the four parallel branch legs are evenly arranged along the pointer, ensuring that the robot is supported by omnidirectional wheel branch legs in all four directions, greatly improving the stability and load-bearing capacity of the mobile robot, while also greatly reducing the risk of interference between the connecting rods of the four parallel branch legs. The two layout methods have their own emphasis, and different layout methods can be adopted according to the requirements of the application scenario.

6. Gait Planning and Simulation Verification

Based on the analysis above, the 8W4L composite mobile robot can switch between two different forms of movement between the wheels and legs. In flat terrain, it is in a wheeled state and can be moved with high maneuverability using omnidirectional wheels. At the same time, due to its eight omnidirectional wheel support chains, it has extremely high load-bearing capacity. The wheeled state does not require gait planning and design. When the robot transitions to legged movement, its leg path needs to be planned and designed. This article takes a typical cross gully terrain as an example to plan and design the cross-gully gait of a symmetrical wheel leg composite mobile robot.

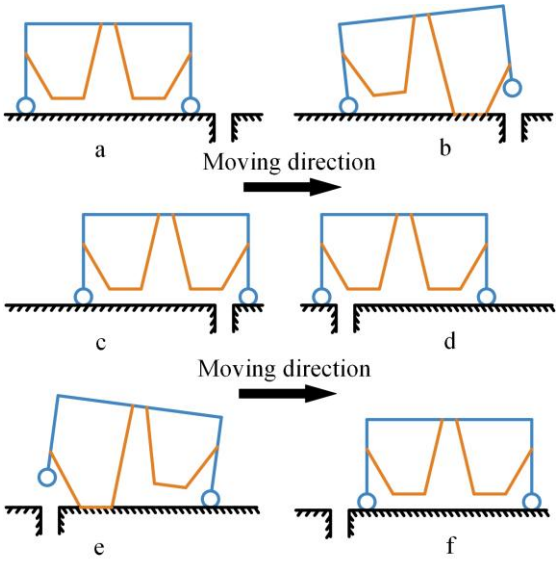

Fig. 8 Robot gully-crossing motion planning

As shown in Fig. 8, the entire process of the mobile robot crossing a gully is completed. On the right side is the forward direction of the robot. Assuming there is a gully with a width of D, for the sake of illustration, two sets of parallel mechanical legs near the forward direction of the robot are defined as a set of branch legs, represented by branch leg I, and two sets of parallel mechanical legs near the forward direction of the robot are defined as a set of branch legs, represented by branch leg II. The specific Fig. 8, a shows the normal state of the robot, which is the wheeled motion mode; Fig. 8, b shows the four front wheels lifted off the ground by the branch leg I. At this point, the mobile robot relies on the support of the branch leg I and the four omnidirectional wheels behind it to coordinate and complete the front wheel crossing action. The robot is in a wheel leg compound movement mode; Fig. 8, c shows the state where the four front wheels are crossed over the gully with the help of the branched leg I, and the robot transitions from the wheel leg compound mode to the wheeled moving state; Fig. 8, d shows the robot moving forward in a wheeled state until the four rear wheels are moved to a position close to the gully; Fig. 8, e is similar to Fig. 8, b, where the four rear wheels are lifted off the ground with the help of the branch leg II. At this point, the mobile robot relies on the support of the branch leg II and the four omnidirectional wheels in front of it to coordinate and complete the rear wheel crossing action. At this point, the robot is in a wheel leg compound movement mode; Fig. 8, f shows the robot completing the cross-gully action and returning to the initial wheeled support state.

From the analysis above, it can be seen that the robot needs two key actions to pass through the gully, which are lifting the front and rear wheels, translating and moving, and completing this action requires parallel support legs to cooperate. Next, taking the rear wheel as an example, as shown in Fig. 8, e, the process of completing the above actions for the parallel mechanism will be designed. During this process, the robot's attitude trajectory mainly lies in the movement trajectory of the foot end. This article mainly focuses on the movement trajectory of the moving wheel, and the foot end trajectory generally includes parabolic, sinusoidal, and linear trajectories. The main movement of mobile robots crossing gullies is in the forward and backward directions. Therefore, we conducted end trajectory analysis on the *YOZ* plane of the mobile robot, with the *Y*-axis pointing towards the forward direction of the robot and the *Z*-axis pointing upwards. Due to the maximum impact on the robot during the lifting and landing of the rear wheels, the instantaneous acceleration required to complete these two actions should be set to 0, and a path movement similar to a sine curve is initially adopted. The mobile end is lifted from its initial position to the highest point and then falls until it reaches the ground. The trajectory path includes up and down movement and forward and backward movement. Complete the process of accelerating and decelerating at the end of the movement in the forward direction, accelerate and decelerate to the highest point in the up and down directions, and reach the endpoint through acceleration deceleration.

Firstly, analyzing the forward and backward motion of a motion cycle, the corresponding acceleration curve can be located as

$$\ddot{y} = A_y \sin\left(\frac{2\pi t}{T}\right). \tag{32}$$

A_y in the equation represents the amplitude, and T represents the time period for the robot to complete one lifting and landing of the moving wheel. The step size from the initial point to the landing point of the moving wheel is set to S. After a series of integration operations and substituting the initial landing parameters, it can be obtained

$$y = S\left(\frac{t}{T} - \frac{1}{2\pi}\sin\frac{2\pi t}{T}\right). \tag{33}$$

When analyzing the vertical direction of the moving wheel, the entire process includes lifting and landing the moving wheel. If these two actions are set as one cycle, it will cause the acceleration to change directly from deceleration to acceleration when passing through the highest point. Considering inertia factors can cause vibration of the robot, affecting its working stability. To avoid this situation, we divide the motion trajectory into three different stage functions, which are specifically represented as

$$\ddot{z}=\begin{cases}A_{za}\sin\left(\dfrac{4\pi t}{T}\right), & 0\le t<\dfrac{T}{4};\\ -A_{zb}\sin\left(\dfrac{2\pi t}{T}-\dfrac{\pi}{2}\right), & \dfrac{T}{4}\le t<\dfrac{3T}{4};\\ A_{zc}\sin\left(\dfrac{4\pi t}{T}-3\pi\right), & \dfrac{3T}{4}\le t\le T.\end{cases} \tag{34}$$

In the equation, A_{za}, A_{zb}, and A_{zc} represent the amplitudes corresponding to different time periods of the function. Based on the preliminary trajectory, it is known that the speed is 0 at the beginning, middle, and end of the cycle. The displacement curve reaches its highest point H at the beginning and end of the cycle, and reaches 0 in the middle. By integrating this equation in a series of steps, we can obtain

$$z=\begin{cases}-\dfrac{H}{\pi+4}\sin\left(\dfrac{4\pi t}{T}\right)+\dfrac{4\pi H}{T(\pi+4)}t,\\ \dfrac{4H}{\pi+4}\sin\left(\dfrac{2\pi t}{T}-\dfrac{\pi}{2}\right)+\dfrac{\pi H}{\pi+4},\\ -\dfrac{H}{\pi+4}\sin\left(\dfrac{4\pi t}{T}-3\pi\right)-\dfrac{4\pi H}{T(\pi+4)}t+\dfrac{4\pi H}{\pi+4}.\end{cases} \tag{35}$$

Based on the comprehensive application scenario settings and the motion performance of the robot, the maximum height of the lifting leg of the robot is set to H=150 mm, the step size is 300 mm, and the set period is 6 s. Without considering the presence of obstacles and other external factors, the set parameters can be substituted into Eqs. (33) and (35) to obtain the movement trajectory curve of the moving wheel.

The motion planning curve of the robot's moving wheel is shown in Fig. 9-12, where Fig. 9 is the specific planning route map in space, Fig. 10 is the schematic diagram of the motion trajectory within *YOZ* when X=100 mm in the workspace, Fig. 11 is the velocity variation curve along the trajectory, and Fig. 12 is the acceleration variation curve along the trajectory.

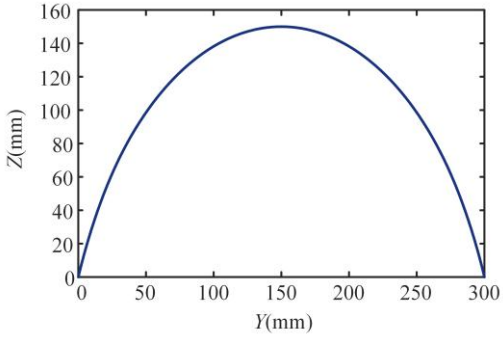

Fig. 9 Rear wheel trajectory

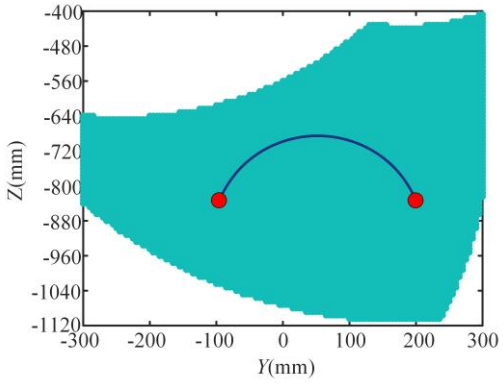

Fig. 10 Trajectory within the workspace

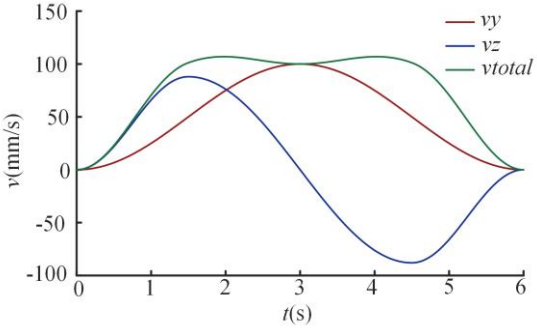

Fig. 11 Rear wheels velocity curves

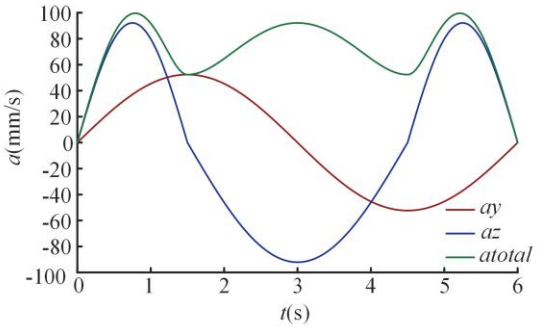

Fig. 12 Rear wheels acceleration curves

By importing the above trajectory planning into MATLAB inverse solution and ADAMS simulation for verification, the length variation curves of each driving rod of a parallel branched leg during the motion process can be obtained. Since this process mainly moves within the *YOZ* plane and there is no movement along the X-axis, it can be inferred that l_3 in this article has not changed and remains at X=100 mm. Fig. 13 shows the length variation curves of three straight rods obtained through MATLAB software, and Fig. 14 shows the length variation curves of three driving rods obtained by importing the resume model into ADAMS software and moving along the planned trajectory.

Observing Fig. 13 and Fig. 14, it is found that when the single branch leg of the wheel leg composite mobile robot moves according to the trajectory planning curve, the length change curve of the robot's drive simulated by MATLAB and ADAMS software basically matches, verifying the feasibility and correctness of the trajectory planning results.

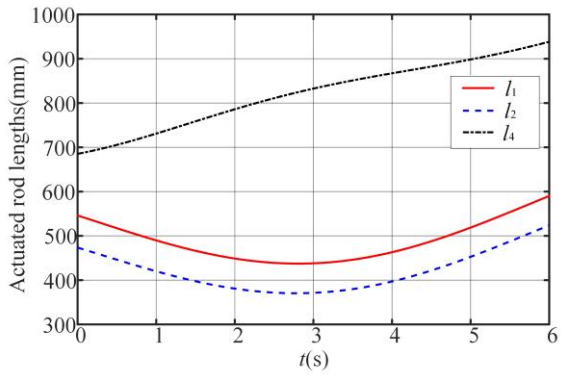

Fig. 13 Variation curve of actuated rod length (MATLAB)

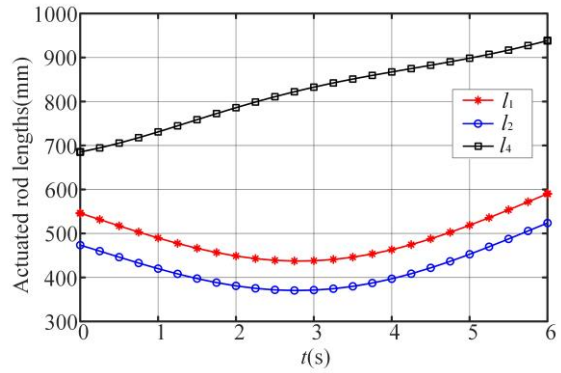

Fig. 14 Variation curve of actuated rod length (ADAMS)

7. Conclusions

This article proposes a novel 8W4L wheel-legged hybrid mobile robot based on a 2-PUS&PRPR parallel mechanism. By combining eight omnidirectional wheels with four sets of parallel branched legs, it achieves three motion modes: full wheel system, leg type, and wheel leg composite.

This article conducted a systematic analysis of the core 2-PUS&PRPR parallel mechanism: based on the screw theory, a degree of freedom analysis was completed to verify its ability to move in three directions and rotate in one axis, totaling four degrees of freedom; Using closed-loop vector method to solve the inverse kinematics, establish the mapping relationship between the driving joint and the end platform; On this basis, a velocity Jacobian matrix is constructed to analyze the singular configuration and motion/force transmission performance, and to clarify the workspace boundary and force transmission characteristics of the mechanism.

Further propose two typical arrangements of parallel mechanisms in mobile robots, and complete gait planning and simulation verification for cross-gully working conditions. The results indicate that the robot significantly improves terrain adaptability and motion stability, providing a theoretical basis for the application of parallel mechanisms in wheel leg composite robots.

Acknowledgements

This research was funded by the Key Research and Development Program of Shanxi Province of China (Grant No. 202202150401018); the Opening Foundation of Shanxi Key Laboratory of Advanced Manufacturing Technology (Grant No. XJZZ202105); and the Central Guidance for Local Science and Technology Development Fund Project (Grant No. YDZJSX2024D079).

References

1. **Mertyüz, İ.; Tanyıldızı, A. K.; Taşar, B.; Tatar, A. B.; Yakut, O.** 2020. FUHAR: A transformable wheel-legged hybrid mobile robot, Robotics and Autonomous Systems 133: 103627. https://doi.org/10.1016/j.robot.2020.103627.
2. **Vatau, S.; Ciupe, V.; Moldovan, C.; Maniu, I.** 2010. Mechanical design and system control of quadruped robot, Mechanika 5(85): 56-60.
3. **Patel, Y.D.; George, P.M.** 2012. Parallel Manipulators Applications – A Survey, Modern Mechanical Engineering 2(3): 57-64. https://doi.org/10.4236/mme.2012.23008.
4. **Ratiu, M.; Anton, D.M.** 2020. A brief overview of parallel robots and parallel kinematic machines, IOP Conference Series: Materials Science and Engineering 898(1): 012007. https://doi.org/10.1088/1757-899X/898/1/012007.
5. **Kim, H. S.; Tsai, L. W.** 2003. Design Optimization of a Cartesian Parallel Manipulator, Journal of Mechanical Design 125(1): 43-51. http://doi.org/10.1115/1.1543977.
6. **Tian, Y.; Zhang, D.; Yao, Y.-A.; Kong, X.; Li, Y.** 2017. A reconfigurable multi-mode mobile parallel robot, Mechanism and Machine Theory 111: 39-65. https://doi.org/10.1016/j.mechmachtheory.2017.01.003.
7. **Chai, C.; Li, R.; Guo, W.; Ning, F.; Zhang, L.** 2026. Integrated design of a hexapod wheel-legged mobile platform and robotic arm based on reconfigurable parallel mechanism, Robotics and Autonomous Systems 202: 105481. https://doi.org/10.1016/j.robot.2026.105481.
8. **Gan, D.; Fu, J.; Lin, H.; Yang, H.; Rastgaar, M.; Min, B.-C.; Voyles, R.** 2022. Actuation-Coordinated Mobile Parallel Robots With Hybrid Mobile and Manipulation Functions, ASME Journal of Mechanisms and Robotics 14(4): 041005. https://doi.org/10.1115/1.4053821.
9. **Carbone, G.; Ceccarelli, M.; Sugahara, Y.; Lim, H. O.; Takanishi, A.** 2006. Stiffness experimental monitoring for WL-16RII Biped Locomotor during walking, Romansy 16: Robot Design Dynamics and Control 487: 105–112. https://doi.org/10.1007/3-211-38927-X_15.
10. **Hashimoto, K.; Sugahara, Y.; Tanaka, C.; Ohta, A.; Hattori, K.; Sawato, T.; Hayashi, A.; Lim, H.; Takanishi, A.** 2007. Unknown disturbance compensation control for a biped walking vehicle, In Proceedings of 2007 IEEE/RSJ International Conference on Intelligent Robots and Systems: 2204-2209. http://doi.org/10.1109/IROS.2007.4399285.
11. **Sugahara, Y.; Carbone, G.; Hashimoto, K.; Ceccarelli, M.; Lim, H. O.; Takanishi, A.** 2007. Experimental Stiffness Measurement of WL-16RII Biped Walking Vehicle During Walking Operation, Journal of Robotics and Mechatronics 19(3): 272-280. https://doi.org/10.20965/jrm.2007.p0272.
12. **Chen, Z.; Wang, S.; Wang, J.; Xu, K.; Lei, T.; Zhang,**

H.; Wang, X.; Liu, D.; Si, J. 2021. Control strategy of stable walking for a hexapod wheel-legged robot, ISA Transactions 108: 367-380. https://doi.org/10.1016/j.isatra.2020.08.033.
13. **Xu, K.; Lu, Y.; Shi, L.; Li, J.; Wang, S.; Lei, T.** 2023. Whole-body stability control with high contact redundancy for wheel-legged hexapod robot driving over rough terrain, Mechanism and Machine Theory 181: 105199. https://doi.org/10.1016/j.mechmachtheory.2022.105199.
14. **Xu, K.; Wang, S.; Wang, J.; Wang, X.; Chen, Z.; Si, J.** 2021. High-adaption locomotion with stable robot body for planetary exploration robot carrying potential instruments on unstructured terrain, Chinese Journal of Aeronautics 34(5): 652-665. https://doi.org/10.1016/j.cja.2020.11.012.
15. **Li, J.; Wu, Q.; Wang, J.; Li, J.** 2021. Neural networks-based sliding mode tracking control for the four wheel-legged robot under uncertain interaction, International Journal of Robust and Nonlinear Control 31: 4306-4323. https://doi.org/10.1002/rnc.5473.
16. **Zhao, Y.; Chai, X.; Gao, F.; Qi, C.** 2018. Obstacle avoidance and motion planning scheme for a hexapod robot octopus-III, Robotics and Autonomous Systems 103: 199-212. https://doi.org/10.1016/j.robot.2018.01.007.
17. **Pan, Y.; Gao, F.** 2015. Kinematic performance analysis for hexapod mobile robot using parallel mechanism, Proceedings of the ASME 2014 International Design Engineering Technical Conferences & Computers and Information in Engineering Conference DETC2014-34591: V05AT08A089. https://doi.org/10.1115/DETC2014-34591.
18. **Xu, Y.; Gao, F.; Pan, Y.; Chai, X.** 2017. Hexapod Adaptive Gait Inspired by Human Behavior for Six-Legged Robot Without Force Sensor, Journal of Intelligent & Robotic Systems 88: 19-35. https://doi.org/10.1007/s10846-017-0532-7.
19. **Du, H.; Gao, F.** 2017. Fault tolerance properties and motion planning of a six-legged robot with multiple faults, Robotica 35(6): 1397-1414. https://doi.org/10.1017/S0263574716000175.
20. **Sang, L.; Wang, H.; Wang, S.; Chen, N.; Wen, Y.** 2014. Theory Analysis and Experiment Research of the Leg Mechanism for the Human-Carrying Walking Chair Robot, Journal of Robotics 2014: 891835. https://doi.org/10.1155/2014/891835.
21. **Wang, H.; Sang, L.; Hu, X.; Zhang, D.; Yu, H.** 2013. Kinematics and dynamics analysis of a quadruped walking robot with parallel leg mechanism, Chinese Journal of Mechanical Engineering 26: 881-891. https://doi.org/10.3901/CJME.2013.05.881.
22. **Wu, G.; Niu, B.** 2024. Hexad robot: a 6-dof parallel PnP robot to accommodate antagonistic rotational capability and structural complexity, Mechanism and Machine Theory 195: 105612. https://doi.org/10.1016/j.mechmachtheory.2024.105612.
23. **Arm, P.; Zenkl, R.; Barton, P.; Beglinger, L.; Dietsche, A.; Ferrazzini, L.; Hampp, E.; Hinder, J.; Huber, C.; Schaufelberger, D.; Schmitt, F.; Sun, B.; Stolz, B.; Kolvenbach, H.; Hutter, M.** 2019. SpaceBok: A Dynamic Legged Robot for Space Exploration, 2019 IEEE/RSJ International Conference on Robotics and Automation (ICRA): 6288-6294. https://doi.org/10.1109/ICRA.2019.8794136.
24. **Wang, J.; Wu, C.; Liu, X.-J.** 2010. Performance evaluation of parallel manipulators: Motion/force transmissibility and its index, Mechanism and Machine Theory 45(10): 1462-1476. https://doi.org/10.1016/j.mechmachtheory.2010.05.001.
25. **Brinker, J.; Corves, B.; Takeda, Y.** 2018. Kinematic performance evaluation of high-speed delta parallel robots based on motion/force transmission indices, Mechanism and Machine Theory 125: 111-125. https://doi.org/10.1016/j.mechmachtheory.2017.11.029.
26. **Olds, K.C.** 2015. Global Indices for Kinematic and Force Transmission Performance in Parallel Robots, IEEE Transactions on Robotics 31(2): 494-500. https://doi.org/10.1109/TRO.2015.2398632.

W. W. Hu, R. Q. Li, D. Lin

PERFORMANCE ANALYSIS OF 8W4L WHEEL-LEGGED HYBRID MOBILE ROBOT WITH PARALLEL MECHANISM

S u m m a r y

This article proposes an 8W4L wheel leg composite mobile robot based on a 2-PUS&PRPR parallel mechanism, equipped with eight omnidirectional wheels and four sets of parallel branched legs, supporting three motion modes: full wheel, leg type, and wheel leg composite. Through the analysis of screw theory, it is concluded that the mechanism has four degrees of freedom, including three directional movement and single axis rotation; Derive the inverse position solution through closed-loop vector method, solve the workspace, and construct the Jacobian matrix to analyze the singular configuration and force transmission performance. The article compares two application modes and applicable scenarios of institutions, completes gait planning for cross gully working conditions, and verifies the effectiveness of the scheme through simulation. Research has shown that the obstacle crossing ability and stability of the robot have been greatly improved, providing a theoretical basis for the application of parallel mechanisms in the field of mobile robots.

Keywords: 2-PUS&PRPR parallel mechanism, performance analysis, gait planning, wheel-legged hybrid mobile robot.

Received June 14, 2026
Accepted October 15, 2026

This article is an Open Access article distributed under the terms and conditions of the Creative Commons Attribution 4.0 (CC BY 4.0) License (http://creativecommons.org/licenses/by/4.0/).